

Domain Imaging in Periodic Submicron Wide Nanostructures by Digital Drift Correction in Kerr Microscopy

Sapida Akhundzada,* Kristina Dingel, David Bischof, Christian Janzen, Bernhard Sick, and Arno Ehresmann

Magneto-optical Kerr microscopy is a powerful method for imaging magnetic domains. Even though domain imaging below the diffractive resolution limit is possible, such investigations are getting increasingly complex with decreasing structure size due to the decreasing Kerr contrast. As magnetic domain images free of topographical artifacts are obtained by subtracting a reference image from the actual image, the corresponding challenges are additionally increased by unavoidable sample motion in the time interval between acquiring the two images. Software-based drift corrections typically rely on a unique structure in the image's region of interest (ROI), recognized automatically or selected manually by the user. By digital image shifting, the ROI positions in the actual and reference images are aligned, and the sample motion is compensated. For magnetic domain imaging in periodically arranged micro- or nano-objects, unique topographical features are not given, making the drift correction by ROIs difficult, often even impossible. Herein, a novel software-based approach is presented for drift corrections to image domains with features close/below the optical resolution limit and for investigating periodically arranged micro- or nano-objects without utilizing ROIs. High-contrast images are obtained, enabling the characterization of periodically arranged 1D, 2D, and 3D magnetic objects with lateral dimensions below 100 nm.

1. Introduction


Magnetic domain imaging techniques link static or dynamically changing magnetic domain configurations to macroscopically averaged properties obtained in magnetization reversal curves recorded by, e.g., alternating gradient,^[1] vibrating sample,^[2] or Kerr magnetometries.^[3–5] The interpretation and modeling of domain images at the surface of a magnetic material increase the understanding of the underlying physical phenomena, starting from fundamental magnetization dynamics to highly evolved application fields like spintronics.^[6] A variety of domain imaging techniques have, therefore, been developed, determining directly local magnetization directions of the domains as a function of the external magnetic field or time.^[3] The most commonly used technique is high-resolution and time-resolved magneto-optical Kerr microscopy, offering high experimental versatility and being compatible with applying external magnetic fields for a large variety of samples.^[3–9] Although domain

imaging by Kerr microscopy is possible for domain sizes beyond the optical resolution limit,^[4] the contrast between such small domains decreases with decreasing domain size. Therefore, technologically more challenging methods like magnetic force,^[10] Lorentz,^[11,12] and X-ray photoemission electron microscopy^[13,14] are often utilized for nanoscale domain imaging. However, domain imaging with these more involved methods is sometimes difficult or even impossible for specific samples or experimental conditions. This motivates work on enhancing the magnetic domain contrast in Kerr microscopy for small-sized domains or for particular domain configurations where standard contrast enhancement methods do not work.

There are three main approaches for enhancing the contrast in Kerr microscopy. A first strategy rests on modifying the experimental setup to be sensitive to different magnetization components with a subsequent subtraction/addition of the signals at different magnetization states,^[7,15] allowing for spatially resolved dynamics analysis^[9,16] or vector imaging of magnetic domains.^[6,7,17,18] In a second approach, the Kerr signal has been enhanced by covering the samples with antireflection layers^[19,20]

S. Akhundzada, D. Bischof, C. Janzen, A. Ehresmann
Institute of Physics and Center for Interdisciplinary Nanostructure Science and Technology (CINSaT)
University of Kassel
34132 Kassel, Germany
E-mail: s.akhundzada@physik.uni-kassel.de

K. Dingel, B. Sick
Intelligent Embedded Systems
University of Kassel
34121 Kassel, Germany

 The ORCID identification number(s) for the author(s) of this article can be found under <https://doi.org/10.1002/adpr.202300170>.

© 2023 The Authors. Advanced Photonics Research published by Wiley-VCH GmbH. This is an open access article under the terms of the Creative Commons Attribution License, which permits use, distribution and reproduction in any medium, provided the original work is properly cited.

DOI: 10.1002/adpr.202300170

or by layers enabling surface plasmon excitation.^[21] A third approach has been the postexperiment digital processing of the images with low Kerr contrast, which can be carried out without any experimental setup or sample modifications. Examples of postprocessing methods for contrast enhancement in digital images are histogram equalization^[22] or genetic algorithms.^[23] As this third approach possesses the potential for contrast enhancement with a minimum of costs, in the current contribution, we will show the feasibility of a postprocessing contrast enhancement method in Kerr microscopy for samples where other standard digital approaches are difficult to apply.

In general, domain observation by Kerr microscopy is facilitated by smooth and optically flat surfaces, as the weak Kerr contrast may be hidden or decreased by strong material or topographic contrast otherwise.^[24] Additionally, inhomogeneous illumination conditions may impede the recording of high-quality Kerr images.^[25] A pure domain image free of contrast due to topographic structures and compensated for laterally varying illumination is, therefore, typically obtained by recording an image at the applied external field H_{ext} , which is then subtracted from a reference image captured at its magnetically saturated state^[25] or by a reference image being averaged during a fast-switching AC loop.^[26]

While the image postprocessing procedures work well for continuous, topographically flat systems, their application to topographically patterned samples is more complex. Difference images, usually obtained in Kerr microscopy measurements, generally suffer from sample motion caused by vibrations, forces due to varying magnetic fields, or varying temperatures, resulting in different positions of the sample in the reference and measurement images. As a consequence, contrast feature artifacts or blurred domains are observed in the difference image, as exemplarily shown in **Figure 1a,b** for exchange biased Cu(5 nm)/IrMn(30 nm)/NiFe(10 nm)/Al(3 nm) microdisks, squares, and stripes with lateral dimensions of 10 μm . The influence of sample motion on the difference image (e.g., being observable as bright and dark artifacts at the structure's edges in **Figure 1a,b**) is increasing with longer acquisition times,

necessary for observing small domains, and with decreasing structure size. In magnetization dynamics experiments, this fact results in varying domain contrast for different sweep rates, complicating their interpretation. Sample motion has been in the past compensated for by a physical repositioning and realigning of the sample back to the position and orientation of the reference image, a method which is also widely used in many biological applications fields.^[27–29] The corresponding position corrections have been achieved experimentally by a feedback loop-controlled xyz-piezo stage mounted beneath the sample holder.^[30,31] For the digital position corrections, pronounced topographic structures on the sample are required and used as markers. Once a marker has been identified, a small section of the image surrounding the marker will be selected as a region of interest (ROI) automatically or manually by the user.^[27,32] For such an ROI, besides containing the topographic features, it is crucial to extend over a sample area where no varying magnetic contrast is expected during the experiment. For flat surfaces without topographic markers or samples with many similar topographic structures, like the periodic topographic patterns of **Figure 1b**, this approach is not or not fully able to compensate for the sample motion.

A standard digital drift correction algorithm generally proceeds in two steps.^[27] In the first step, after selecting the marker and the corresponding ROI, the translational drift of the measurement image concerning the reference image is detected by comparing the positions and orientations of the marker within the ROI. The marker motion between the measurement and reference images can be determined in the simplest case by taking the sum of the squared gray scale differences between the actual image and reference over all pixels in the ROI. During this template-matching procedure, the ROI is shifted from the actual image's position toward the ROI's position in the reference image. At the position of a minimum difference, the shift parameters are determined, which are then used to match the images in the second step of the drift correction.^[33] The computational time depends on the number of individual images in the image series, the area of the selected ROI, and the desired accuracy.^[27]

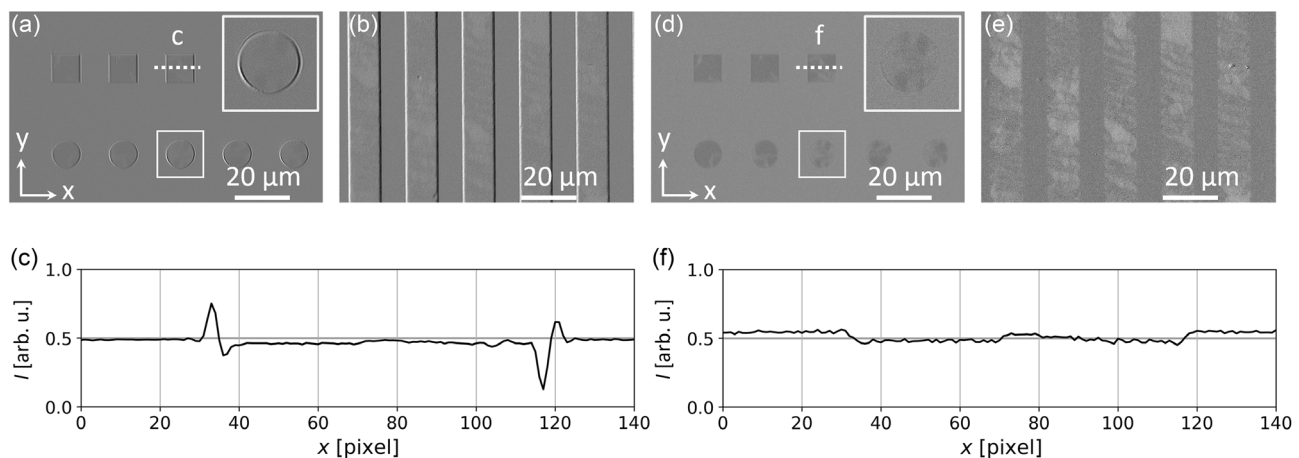


Figure 1. Kerr microscopic difference images obtained by background subtraction of 2D and 1D periodic Cu/IrMn/NiFe/Al microstructures without drift correction (a,b) and with drift correction (d,e). The magnified inlet figure in (a) shows how the relative motion of the sample enhances the contrast at the structure edges, while the drift-corrected one in (d) is a pure domain image. Subfigures (c,f) shows the intensity cross-section of the microsquare along the dotted lines in (a) and (d).

Selecting a unique topographic marker and the corresponding ROI for topographically elevated periodic magnetic microstructures is difficult. For example, for periodic 1D structures, a 2D repositioning fails due to the translational symmetry along the nonperiodic axis (in the case of Figure 1b the y -axis). To avoid these difficulties, we developed a drift correction algorithm with the open-source program language Python in which a manual or automated selection of a ROI with a unique topographic marker is not necessary and it works well with topographically elevated micro- and nanostructures. To demonstrate the power of the newly developed shift correction code, the processing of Kerr images will be compared to the results of standard image processing.

2. Results and Discussion

A high-resolution Kerr microscope with eight white light-emitting diodes^[6] and an installed digital CMOS camera captured the Kerr images. Using a 100x objective, one pixel corresponds to about 50 nm². Pixel intensities are delivered by the camera in the 12-bit and stored in a linear 16-bit scale in the images displayed as grayscale ranging from $g_{\min} = 0$ to $g_{\max} = 65535$. The recorded image files in .png format were converted to NumPy arrays^[34] of 642×960 pixels. The contrast and dynamic range of individual recorded images have been optimized by the following procedure:

1) The acquisition time of the CMOS camera in combination with the analyzer angle has been varied such that the average grayscale $g_{\text{av}} = \frac{1}{642} \cdot \frac{1}{960} \sum_{h=1}^{642} \sum_{j=1}^{960} g_{h,j}$ lies approximately in the middle of the 16-bit grayscale range. For the current experiments, the dynamic grayscale range $[g_{\text{topo,max}}, g_{\text{topo,min}}]$ from the topographic structures is larger than the one for the magnetic signal variations $[g_{\text{magn,max}}, g_{\text{magn,min}}]$, i.e., $g_{\text{topo,min}} < g_{\text{magn,min}} < g_{\text{magn,max}} < g_{\text{topo,max}}$. The grayscale ranges, set this way, avoid an influence of the magnetic domain appearance on the topographic drift correction and have been fixed for the entire image gray level range during further image processing.

2) Inhomogeneous illumination conditions are eliminated by subtracting a reference image from the actual (shift-corrected) measurement images. The difference data are used in their raw format with original pixel intensity values during the complete image processing. Image processing causing a change of the individual pixel intensity values by noise filters, histogram equalization, or blurring operations is not conducted at all.

3) Even though the current shift correction code does not require topographic markers with unique structural features, the presence of topographic structures on the sample surface is indispensable (e.g., dust, defects, or topographically elevated (periodic) structures). Minor intensity differences caused by a topographic contrast are sufficient for precise 2D repositioning. However, the current drift correction code does not work for entirely flat or smooth surfaces.

Algorithm 1 presents the drift correction code, which is applied to each image of a measurement series. A detailed description of Algorithm 1 in the open-source program language Python is provided in the Supporting Information, available from the Wiley Online Library or the author. Starting with an individual recorded image \mathbf{X}_{rec} , this image is shifted along an axis a in a

Algorithm 1. Drift correction for a single image.

```

procedure ShiftCorr( $\mathbf{X}_{\text{ref}}, \mathbf{X}_{\text{rec}}, \mathcal{A}$ ) ▷  $\mathcal{A} \leftarrow \{\text{hor, ver}\}$ 
  for each  $a \in \mathcal{A}$  do
    axis_shift_index  $\leftarrow 0$ 
    last_cost  $\leftarrow \text{MSD}(\mathbf{X}_{\text{ref}}, \mathbf{X}_{\text{rec}})$ 
    current_cost  $\leftarrow \infty$ 
    do
      if current_cost  $\neq \infty$  then
        last_cost  $\leftarrow$  current_cost
      end if
       $i \leftarrow \text{select\_next\_shift\_candidate}()$  ▷  $i \in \mathbb{R}$ 
       $\mathbf{X}_{\text{shift},i} = \text{shift\_image}(\mathbf{X}_{\text{ref}}, \mathbf{X}_{\text{rec}}, a, i)$ 
      current_cost = MSD( $\mathbf{X}_{\text{ref}}, \mathbf{X}_{\text{shift},i}$ )
      axis_shift_index  $\leftarrow i$ 
    while last_cost > current_cost
     $\mathbf{X}_{\text{shift}} = \text{shift\_image}(\mathbf{X}_{\text{ref}}, \mathbf{X}_{\text{rec}}, a, \text{axis\_shift\_index})$ 
  end for
  return  $\mathbf{X}_{\text{shift}}$ 
end procedure

```

set \mathcal{A} such the mean squared deviation (MSD, Equation (1)) between the reference \mathbf{X}_{ref} and moved recorded image $\mathbf{X}_{\text{shift}}$, defined as the cost function, is minimized. Function *select_next_shift_candidate* estimates the next shifting index i based on constrained optimization by linear approximation^[35] for both axes a in \mathcal{A} and is used to shift the image \mathbf{X}_{rec} to form a shifted image $\mathbf{X}_{\text{shift},i}$.

$$\text{MSD}(\mathbf{X}_{\text{ref}}, \mathbf{X}_{\text{shift},i}) = \frac{1}{m \cdot n} \sum_{h=1}^m \sum_{j=1}^n (\mathbf{X}_{\text{ref},h,j} - \mathbf{X}_{\text{shift},i,h,j})^2 \quad (1)$$

Here, (h, j) represents a pixel value within the provided image and $m \cdot n$ represents the total number of pixels within \mathbf{X} . This procedure is repeated until the MSD is minimal, and the algorithm returns the image $\mathbf{X}_{\text{shift}}$ with compensated translational motion along a . The whole procedure is an optimization problem where the mean squared deviation as a cost function is minimized. The advantage of using this procedure is that it can be applied with subpixel accuracy, meaning that $i \in \mathbb{R}$. The new intensity values for subpixel shifts are calculated by spline interpolation.^[36]

Finally, the difference image between $\mathbf{X}_{\text{shift}}$ and \mathbf{X}_{ref} is calculated for contrast enhancement of the magnetic domains. The grayscale $g_{m,n,\text{norm}}$ for each pixel (m, n) in the difference image has been chosen to be linear and normalized to values between 0 and 1.

Figure 1d,e presents the Kerr images of Figure 1a,b with compensated sample drift of the measurement image by 0.86 pixel along the horizontal and 0.27 pixel along the vertical axis, calculated by Algorithm 1. In comparison to Figure 1a,b, which are based on the standard image processing, Figure 1d,e shows pure domain images free of topographical contrast.

Algorithm 1 is also capable to also compensate for the sample motion in periodic 1D nanostructures with small periodicities,

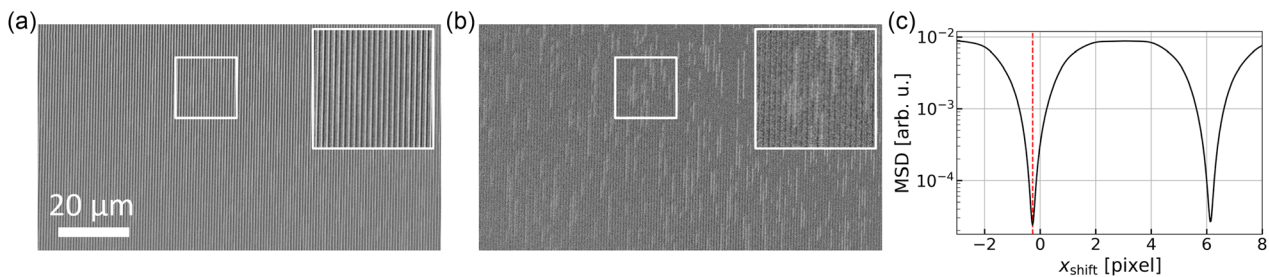


Figure 2. Kerr microscopic difference images a) without and b) with drift correction of nominally 250 nm wide Ti/Au/Co/NiO nanostructures of 500 nm periodicity. Due to the sample motion, the magnetic domains become only visible in the drift-corrected difference image. c) Dependence of the MSD on the displacement between the reference image and the actual one along the x-axis. The global minimum at -0.14 pixels indicates a lateral drift of 7 nm, which need to be corrected. The local minimum at 6.24 pixels (corresponding to 312 nm) indicates the true periodicity of 319 nm ($=312 \text{ nm} + 7 \text{ nm}$) of the nominally 250 nm wide parallel stripes. Note the logarithmic scale of the plotted data.

while in standard image processing, this is difficult. **Figure 2** shows the Kerr microscopic difference images of 250 nm wide magnetic nanostructures arranged in a periodic array with a periodicity of 500 nm. Even though the Ti(4 nm)/Au(60 nm)/Co(0.8 nm)/NiO(5 nm) nanostructures exhibit a perpendicular magnetization, having a stronger Kerr contrast than in-plane magnetized layer systems,^[3] nearly no magnetic domains are visible in the difference image in **Figure 2a**. Due to the sample moving along the horizontal axis, the stripes' edges in the reference image overlap with the magnetic domains inside the stripes in the measurement image. In **Figure 2b**, the sample drift in the measurement image concerning the reference image was calculated and compensated for using Algorithm 1. In the resulting difference image, the magnetic domains become visible, free from topographic artifacts. Based on the given periodicity, several minima are calculated by the MSD with one global minimum at the position of -0.14 pixel, corresponding to the initial position of the measurement image to the reference image.

Resolving magnetic domains in 250 nm wide nanostructures is close to the optical resolution limit when using white light microscopy.^[37] The resolution limit can be further minimized to up to 150 nm when using the blue spectral lines (404 and 435 nm) of a mercury arc high-pressure lamp.^[4] So far, small domains were imaged magneto-optically in 400 nm embedded perpendicularly magnetized nanowires^[38] or in 300 nm wide topographically elevated nanowires being part of a larger polygon,^[39] with clear image and edge contrast. Smaller objects like in-plane magnetized vortex domain walls in 310 nm wide amorphous stripes, perpendicularly magnetized skyrmion bubble domains with varying diameters between 50 and 450 nm^[40] or 50 nm wide perpendicularly magnetized nanowires^[4] were captured by Kerr microscopy. However, depending on the structure width, the visibility of the domains is limited by the reflected intensity of the objects.^[4]

In further experiments by other authors, the Kerr signal was obtained for measuring single-pass hysteresis loops of an individual 30 nm wide cobalt wire, but besides magnetometry, domain imaging was not possible.^[41] Beyond this resolution limit, Kerr microscopy has been utilized to quantitatively determine the size of crucial subresolution-sized embedded magnetic domains based on the integral-contrast method after normalization to the maximum domain contrast.^[40] Considering the

intensity plot shown in **Figure 1c**, the material contrast, coming from the nanostructure's edges, overlaps and alters the maximum domain contrast, making this method currently not feasible for elevated nanostructures. For analyzing the limitations of the presented drift correction algorithm in correlation with magnetic domains in the subresolution regime, topographically elevated Cu/IrMn/NiFe/Al nanostructures with lateral dimensions varying between 1 μm and 70 nm have been fabricated. Note two crucial experimental restrictions: 1) For imaging magnetic domains with maximum contrast, the nanostructures were designed to be not closer together than the resolution limit of 250 nm. 2) To minimize the focus drift, distorting the magnetic domain's visibility in the difference image, the reference and measurement images were captured in a short acquisition time.

The resulting Kerr difference images are shown in **Figure 3**. While the upper row presents the difference images based on the standard image processing, the images in the lower row are calculated using the drift correction of Algorithm 1. In the first row magnetic domains are visible in the nanostructures with widths larger than 250 nm. In these images, the sample motion is observable as artificial contrast features in the regions with no magnetization reversal. In comparison, the images in the second row do not indicate any influence of sample motion on the difference images. In the case of the 1 μm wide stripes, a moving domain with low grayscale intensity is visible, while this information is suppressed in the noncorrected images by the artificial contrast features. Starting from 250 nm, the contrast of the magnetic domains for the images in the first row decreases with decreasing stripe width until they are not visible below 125 nm. When the sample motion is compensated, the domain contrast is visible until the nanostructures have a lateral dimension of 80 nm. In the case of the 70 nm wide nanostructures, the magnetic domains are visible blurrily. Here, the contrast can be further enhanced digitally by histogram equalization.

In the last experiment, the feasibility of the drift algorithm in combination with 3D microstructures is examined. In this analysis, hemispherical tori arranged in periodic arrays with varying lattice geometry, as shown in the scanning electron micrograph (SEM) in **Figure 4a**, is characterized by Kerr microscopy using 50 \times and 100 \times objectives. These kinds of structures are interesting for application technologies, as in 3D nanostructures the inversion symmetry breaking results from curvature-induced

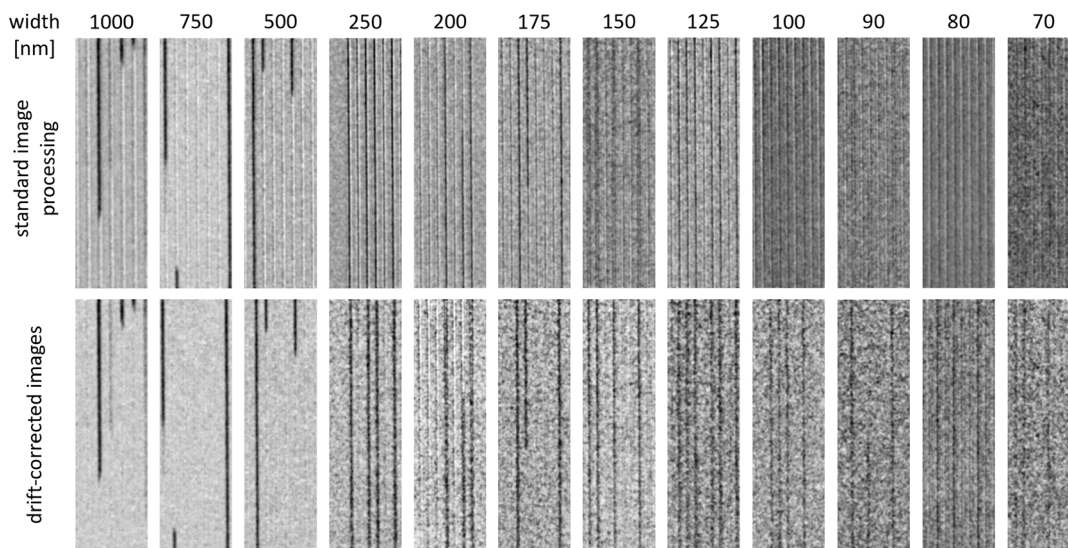


Figure 3. Comparison of nonmodified and drift-corrected Kerr microscopic difference images of stripes with lateral dimensions varying between 1 μm and 70 nm.

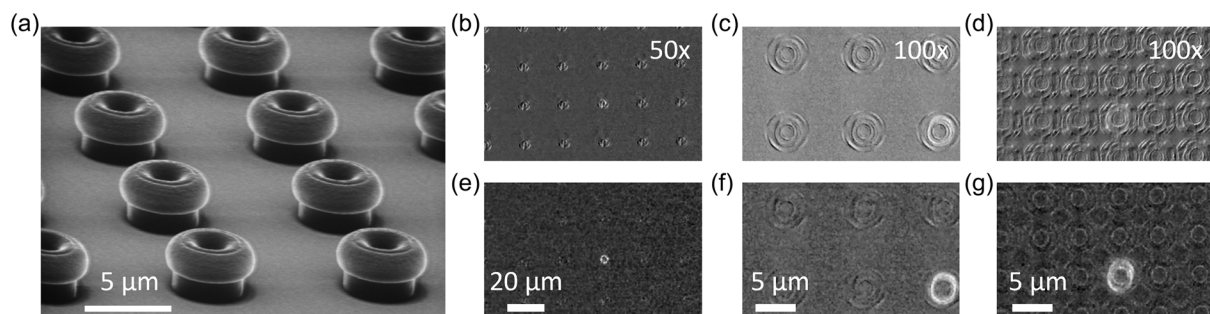


Figure 4. a) SEM micrograph of 3D hemispherical tori. b–d) While in the nonmodified Kerr difference images the magnetic domains are partly suppressed by the sample motion and focus drift, e–g) the remagnetized white domains are visible in the digitally drift-corrected Kerr microscopic difference images.

effects, essential for the stabilization of topological nontrivial spin textures in symmetric material systems.^[42–44] The Kerr magnetometry and microscopy experiments of these 3D structures are challenging because light diffraction and scattering reduce the Kerr signal. In Figure 4b–d, the magnetic domains in the Kerr difference images are distorted by the sample drift accompanied by the additional focus drift, making the evaluation of these data impossible. In Figure 4e–g, the obtained measurement images were aligned to the reference image using the presented drift algorithm. Domain images with high image contrast and free of topographical information can be captured using the 50 \times objective (Figure 4e). However, when using the 100 \times objective (Figure 4f,g) the focus drift prevents a perfect alignment of the reference and measurement images.

3. Conclusion

In summary, we have presented a drift correction algorithm correcting the sample motion in Kerr microscopic images, essential for magnetic domain imaging in magnetic 1D, 2D, and 3D

micro- and nanostructures. The drift correction algorithm can be implemented using Python or other programming languages, and it leaves room for improvements by using mathematically more sophisticated cost functions instead of the MSD. Using the drift correction, magnetic domains can be captured in nanostructures with lateral dimensions up to 80 nm beyond the optical resolution limit. Compared to other drift correction algorithms based on the selection of ROIs, our drift correction algorithm works well with periodic micro- and nanostructure. This method can also be used in other scientific fields where sample motions need to be compensated for superresolution and superaccuracy studies with minimal computational demands. Future works focus on implementing the drift correction code into the live imaging during the experimental image acquisition.

Supporting Information

Supporting Information is available from the Wiley Online Library or from the author.

Acknowledgements

The authors acknowledge the fruitful discussions with *Evico magnetics* GmbH (<http://www.evico-magnetics.de>), Rudolf Schäfer (Leibniz Institute for Solid State and Materials Science (IFW) Dresden, Institute for Materials Science, TU Dresden), Ivan Soldatov (Leibniz Institute for Solid State and Materials Science (IFW) Dresden), Michael Vogel (Institute for Materials Science, Kiel University), and Marco Stein (University of Kassel). The authors further acknowledge the support by Piotr Kuświk and Michał Matczak (Institute of Molecular Physics, Polish Academy of Sciences) for providing the layer systems and by Annette Becker (Institute of Physics and Center for Interdisciplinary Nanostructure Science and Technology (CINSA-T), University of Kassel) in the fabrication of the lithographic structures. S. A. acknowledges gratefully support by the Ph.D. scholarship fund of Kassel University. B. S. and A. E. gratefully acknowledge support by the joint Lab "Artificial Intelligence Methods for Experiment Design (AIM-ED)" of Helmholtzzentrum für Materialien und Energie, Berlin and Kassel University.

Open Access funding enabled and organized by Projekt DEAL.

Conflict of Interest

The authors declare no conflict of interest.

Data Availability Statement

The data that support the findings of this study are available from the corresponding author upon reasonable request.

Keywords

drift correction, image processing, imaging methods, Kerr microscopy, magnetic domain imaging, optical microscopy, resolution limit

Received: May 30, 2023

Revised: August 2, 2023

Published online: August 27, 2023

- [1] P. J. Flanders, *J. Appl. Phys.* **1988**, 63, 3940.
- [2] S. Foner, *Rev. Sci. Instrum.* **1959**, 30, 548.
- [3] A. Hubert, R. Schäfer, *Magnetic Domains*, Springer, Berlin, Heidelberg **2009**, ISBN 978-3-540-64108-7.
- [4] R. Schäfer, J. McCord, *Magneto-Optical Microscopy*, Springer International Publishing, Cham, Switzerland **2021**, pp. 171–229, ISBN 978-3-030-70443-8.
- [5] I. Soldatov, P. Andrei, R. Schaefer, *IEEE Magn. Lett.* **2020**, 11, 2405805.
- [6] I. V. Soldatov, R. Schäfer, *Rev. Sci. Instrum.* **2017**, 88, 7.
- [7] I. V. Soldatov, R. Schäfer, *Phys. Rev. B* **2017**, 95, 014426.
- [8] R. Schäfer, in *Handbook of Magnetism and Advanced Magnetic Materials*, John Wiley & Sons, Hoboken, NJ **2007**, <https://doi.org/10.1002/9780470022184.hmm310>.
- [9] J. McCord, *J. Phys. D: Appl. Phys.* **2015**, 48, 333001.
- [10] U. Hartmann, *Modern Techniques for Characterizing Magnetic Materials*, Springer, New York, NY **2005**, pp. 411–451.
- [11] C. Phatak, A. K. Petford-Long, M. De Graef, *Curr. Opin. Solid State Mater. Sci.* **2016**, 20, 107.
- [12] J. Zweck, T. Zimmermann, T. Schuhrke, *Ultramicroscopy* **1997**, 67, 153.
- [13] A. Scholl, H. Ohldag, F. Nolting, J. Stöhr, H. A. Padmore, *Rev. Sci. Instrum.* **2002**, 73, 1362.
- [14] P. Fischer, *IEEE Trans. Magn.* **2015**, 51, 2.
- [15] T. Von Hofe, N. Onur Urs, B. Mozooni, T. Jansen, C. Kirchhof, D. E. Bürgler, E. Quandt, J. McCord, *Appl. Phys. Lett.* **2013**, 103, 142410.
- [16] T. Henn, T. Kiessling, W. Ossau, L. W. Molenkamp, K. Biermann, P. V. Santos, *Rev. Sci. Instrum.* **2013**, 84, 12.
- [17] R. B. Holländer, C. Müller, M. Lohmann, B. Mozooni, J. McCord, *J. Magn. Magn. Mater.* **2017**, 432, 283.
- [18] W. Rave, R. Schäfer, A. Hubert, *J. Magn. Magn. Mater.* **1987**, 65, 7.
- [19] D. Kim, Y. W. Oh, J. U. Kim, S. Lee, A. Baucour, J. Shin, K. J. Kim, B. G. Park, M. K. Seo, *Nat. Commun.* **2020**, 11, 5937.
- [20] J. Kranz, A. Hubert, *Z. Angew. Phys.* **1963**, 15, 220.
- [21] A. A. Grunin, A. G. Zhdanov, A. A. Ezhov, E. A. Ganshina, A. A. Fedyanin, *Appl. Phys. Lett.* **2010**, 97, 26.
- [22] M. Abdullah-Al-Wadud, M. Kabir, M. Akber Dewan, O. Chae, *IEEE Trans. Consum. Electron.* **2007**, 53, 593.
- [23] S. Hashemi, S. Kiani, N. Noroozi, M. E. Moghaddam, *Pattern Recognit. Lett.* **2010**, 31, 1816.
- [24] I. Soldatov, V. Kolesnikova, V. Rodionova, R. Schaefer, *IEEE Magn. Lett.* **2021**, 12, 2021.
- [25] F. Schmidt, W. Rave, A. Hubert, *IEEE Trans. Magn.* **1985**, 21, 1596.
- [26] M. Jovicevic-Klug, P. Jovicevic-Klug, J. McCord, B. Podgornik, *J. Mater. Res. Technol.* **2021**, 11, 1245.
- [27] B. Schaffer, W. Grogger, G. Kothleitner, *Ultramicroscopy* **2004**, 102, 27.
- [28] M. J. Mlodzianoski, J. M. Schreiner, S. P. Callahan, K. Smolková, A. Dlasková, J. Šantorová, P. Ježek, J. Bewersdorf, *Opt. Express* **2011**, 19, 15009.
- [29] M. Beckers, T. Senkbeil, T. Gorniak, K. Giewekemeyer, T. Salditt, A. Rosenhahn, *Ultramicroscopy* **2013**, 126, 44.
- [30] A. R. Carter, G. M. King, T. A. Ulrich, W. Halsey, D. Alchenberger, T. T. Perkins, *Appl. Opt.* **2007**, 46, 421.
- [31] L. Nugent-Glandorf, T. T. Perkins, *Opt. Lett.* **2004**, 29, 2611.
- [32] S. H. Lee, M. Baday, M. Tjioe, P. D. Simonson, R. Zhang, E. Cai, P. R. Selvin, *Opt. Express* **2012**, 20, 12177.
- [33] J. Sarvaiya, S. Patnaik, S. Bombaywala, in *2009 Int. Conf. Advances in Computing, Control, and Telecommunication Technologies*, Vol. 3, IEEE, Piscataway, NJ **2009**, pp. 819–822, ISBN 978-1-4244-5321-4.
- [34] C. R. Harris, K. J. Millman, S. J. van der Walt, R. Gommers, P. Virtanen, D. Cournapeau, E. Wieser, J. Taylor, S. Berg, N. J. Smith, R. Kern, M. Picus, S. Hoyer, M. H. van Kerkwijk, M. Brett, A. Haldane, J. F. del Río, M. Wiebe, P. Peterson, P. Gérard-Marchant, K. Sheppard, T. Reddy, W. Weckesser, H. Abbasi, C. Gohlke, T. E. Oliphant, *Nature* **2020**, 585, 357.
- [35] M. Powell, *Nonlinear Programming*, Vol. 3, Elsevier, Amsterdam/New York **1978**, pp. 27–63.
- [36] D. Han, in *Proc. 2nd Int. Conf. Computer Science and Electronics Engineering (ICCSEE 2013)*, Atlantis Press, Paris, France **2013**, pp. 1556–1559, ISBN 978-90-78677-61-1.
- [37] F. R. S. Lord Rayleigh, *Lond. Edinb. Dublin Philos. Mag. J. Sci.* **1879**, 8, 261.
- [38] J. P. Jamet, J. Ferré, P. Meyer, J. Gierak, C. Vieu, F. Rousseaux, C. Chappert, V. Mathet, *IEEE Trans. Magn.* **2001**, 37, 2120.
- [39] E. Lage, R. Mattheis, J. McCord, *J. Magn. Magn. Mater.* **2019**, 487, 165273.
- [40] I. V. Soldatov, W. Jiang, S. G. Te Velthuis, A. Hoffmann, R. Schäfer, *Appl. Phys. Lett.* **2018**, 112, 262404.
- [41] E. Nikulina, O. Idigoras, P. Vavassori, A. Chuvilin, A. Berger, *Appl. Phys. Lett.* **2012**, 100, 14.
- [42] S. Vojkovic, A. S. Nunez, D. Altbir, V. L. Carvalho-Santos, *J. Appl. Phys.* **2016**, 120, 3.
- [43] V. P. Kravchuk, U. K. Rößler, O. M. Volkov, D. D. Sheka, J. Van Den Brink, D. Makarov, H. Fuchs, H. Fangohr, Y. Gaididei, *Phys. Rev. B* **2016**, 94, 144402.
- [44] R. G. Elías, N. Vidal-Silva, V. L. Carvalho-Santos, *Sci. Rep.* **2019**, 9, 14309.